Optimized Reactive Power Flow of DFIG Power Converters for Better Reliability Performance Considering Grid Codes

Dao Zhou, *Student Member, IEEE*, Frede Blaabjerg, *Fellow, IEEE*, Mogens Lau, and Michael Tønnes

***Abstract*—If there is no reactive power exchange between a doubly fed induction generator (DFIG) and a grid, the various characteristics of the power converters in a DFIG wind turbine system cause the lifetime expectancy of a rotor-side converter (RSC) to be significantly less than that of a grid-side converter (GSC). In order to fulfill modern grid codes, over-excited reactive power injection will further reduce the lifetime of the RSC. In this paper, the additional stress of a power semiconductor due to the reactive power injection is first evaluated in terms of a modulation index and the current loading. Then, an optimized reactive power flow is proposed in the case where an over-excited reactive power support is applied with the joint compensation from both the RSC and the GSC. Finally, some experimental validations are performed at a downscale DFIG prototype. It is concluded that, among the different combined reactive power support strategies, the best scheme will tradeoff the lifetime between the GSC and the RSC.**

***Index Terms*—Consumed lifetime, doubly fed induction generator (DFIG), reactive power, thermal behavior.**

I. Introduction

THE worldwide wind capacity reached close to 320 GW by the end of 2013 [1]. As a modern wind turbine is required to act similar to a conventional synchronous generator with independent reactive power and active power regulation in order to handle power quality issues [2], power electronics are nowadays playing a more important role even to the full scale of a wind turbine generator (e.g., a permanent-magnet synchronous generator). In order to reduce the cost of wind power generation, the power rating of the wind turbine is now upscaling to 8 MW. However, the feedback of the wind turbine market indicates that the best seller is still that rated around 2–3 MW, in which a doubly fed induction generator (DFIG) is normally employed together with partial-scale power electronic converters [3]–[6].

Manuscript received November 18, 2013; revised March 8, 2014, June 11, 2014, and July 30, 2014; accepted August 31, 2014. Date of publication September 24, 2014; date of current version February 6, 2015.

D. Zhou and F. Blaabjerg are with the Department of Energy Technology, Faculty of Engineering and Science, Aalborg University, 9220 Aalborg, Denmark (e-mail: zda@et.aau.dk; fbl@et.aau.dk).

M. Lau is with Siemens Wind Power A/S, 7330 Brande, Denmark (e-mail: mogens.lau@siemens.com).

M. Tønnes is with Danfoss Silicon Power GmbH, 24941 Flensburg, Germany (e-mail: michael.tonnes@danfoss.com).

Color versions of one or more of the figures in this paper are available online at http://ieeexplore.ieee.org.

Digital Object Identifier 10.1109/TIE.2014.2359911

Another progress in the wind turbine technology is the movement of wind farms from onshore to offshore to reduce the environment impact and to obtain even better wind conditions. Because of the expensive maintenance for offshore wind farms, the lifetime of the whole system normally preserves 20–25 years, which is much longer than the traditional industrial standard [7]. Consequently, the reliability of an offshore wind turbine system becomes of interest from the manufacturer's perspective. As the state-of-the-art agreement, the reliability engineering in power electronics is currently moving from a solely statistical approach to a more physics-based approach, which involves not only the statistics but also the root cause behind the failures [8]–[13].

Considerable reliability tests have been already carried out by leading power semiconductor manufacturers. In [14] and [15], the power cycles of a power device are provided in traction systems from a thermal stress point of view, and the most important factors affecting the lifetime are summarized in [16] (e.g., mean junction temperature, junction temperature fluctuation, the ON-state time duration of a periodical current, etc.). A lot of papers also address the reliability issues in wind turbine systems [17]–[20], which implies that the thermal cycles of a power semiconductor generally include small cycles (e.g., current commutation within one fundamental frequency) and large cycles (e.g., the fluctuation of wind speed and environment temperature). This paper mainly focuses on the steady-state small thermal cycles. In the DFIG system, as a rotor-side converter (RSC) and a grid-side converter (GSC) are both able to provide the reactive power support, thereby, the total minimum power can be achieved by using a proper reactive power share, which can enhance the system efficiency [21], [22]. Moreover, due to the various characteristics of the power converters in the DFIG system, it can be also seen that the lifetime expectancy between the RSC and the GSC could be also significantly unequal. This paper investigates a smart reactive power share between back-to-back (BTB) power converters in order to balance their lifetime seen from the thermal stress of the power semiconductor.

The layout of this paper is organized as follows. In Section II, the loss breakdown and the thermal behavior of the power device are estimated at some typical wind speeds; thus, the consumed lifetime of the power converters can be obtained based on an annual wind profile. Section III describes the additional stress of the power device introduced by the reactive power support required by the modern grid codes. In Section IV, as the reactive power can be supplied either from the GSC

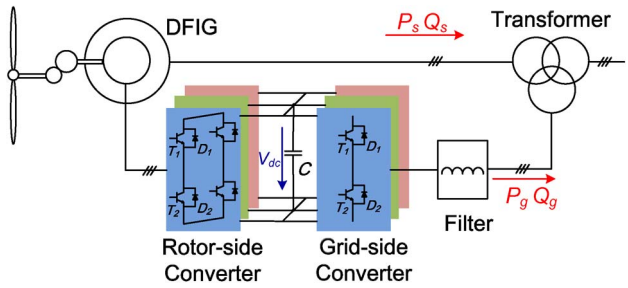

Fig. 1. DFIG-based wind energy generation system.

or the RSC, different combined reactive power compensation strategies are adopted in order to seek the best solution for the DFIG system with respect to the lifetime expectancy of the power converters. In Section V, the experimental results of the reactive power compensation strategies are tested in a downscale DFIG system. Finally, some conclusions are drawn in Section VI for controlling this system.

II. Various Characteristics of BTB Power Converters With Respect to Reliability

The typical configuration of a DFIG-based wind turbine system is shown in Fig. 1. As the BTB power converters have different performances (e.g., the control objectives, the interface voltages, and the operational frequencies), different loss distributions in the power semiconductors can be expected; thus, various thermal profiles inevitably induce an unbalanced lifetime between the GSC and the RSC. Based on a typical annual wind profile, this section will evaluate the estimated lifespan of the power electronic converters.

A. Loss Breakdown of Power Device

The power loss of the power device mainly includes the conduction loss and the switching loss [23]. The conduction loss in each power device P_{con} can be deduced as [24]

$$P_{\text{con}} = f \cdot \left(\sum_{n=1}^{N} v_{CE}\left(|i_a(n)|\right) \cdot |i_a(n)| \cdot T_1(n) + \sum_{n=1}^{N} v_F\left(|i_a(n)|\right) \cdot |i_a(n)| \cdot \left(T_s - T_1(n)\right) \right) \quad (1)$$

where the first term is the conduction loss of the insulated-gate bipolar transistor (IGBT) T_{con}, and the second term is the conduction loss of the freewheeling diode D_{con}. i_a is the sinusoidal current through the power device, T_1 is the ON time of the upper leg within a switching period T_s (in Fig. 1), and v_{CE} and v_F are the voltage drops of the IGBT and the diode, respectively, during their ON-state period, which are normally given by the manufacturer. N is the carrier ratio, whose value is the switching frequency over fundamental frequency f, and subscript n is the nth switching pattern.

The space vector modulation is widely used in a three-phase three-wire system due to its higher utilization of the dc-link voltage. In order to guarantee the minimum harmonic, the symmetrical sequence arrangement of the no-zero vector and the zero vector is normally used, and the conduction time of the upper and lower switches of the leg can be thus deduced based on the voltage angle [25]. Within one fundamental frequency of the converter output current, each IGBT in a leg always only conducts half-period. The direction of the current is relevant to the conduction loss distribution between the IGBT and the diode. As a result, the phase angle between the converter voltage and the current is also important.

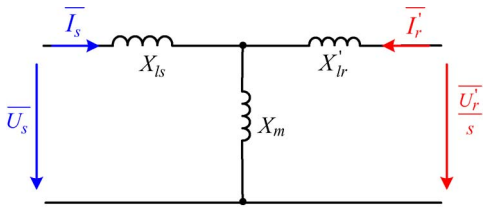

Fig. 2. One-phase DFIG equivalent circuit in the phasor diagram.

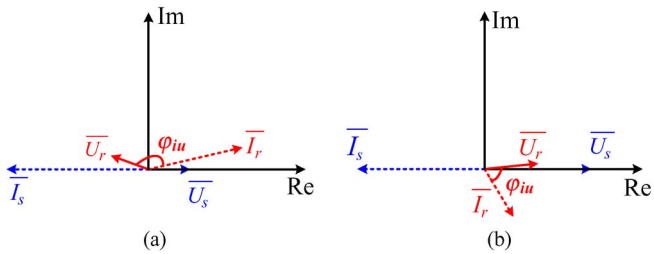

Fig. 3. Phasor diagram of the stator voltage, the stator current, the rotor voltage, and the rotor current. (a) Supersynchronous mode. (b) Subsynchronous mode.

For the RSC, the phase angle is related to the power factor of the stator side of the DFIG and the DFIG instinctive parameters. Neglecting the stator resistance and the rotor resistance, the steady-state DFIG equivalent circuit is shown in Fig. 2 in terms of the phasor expression.

Taking phase A as an example, if the stator voltage is assumed as the reference direction and all quantities are transferred to the stator side, the voltage and current relationships between the rotor side and the stator side are

$$\overline{I_r'} = -\frac{X_s}{X_m} I_{s\_\text{Re}} + j \cdot \text{sign}(s) \cdot \left(-\frac{U_{s\_\text{Re}}}{X_m} - \frac{X_s}{X_m} I_{s\_\text{Im}} \right) \quad (2)$$

$$\overline{U_r'} = s \cdot \left(\frac{X_r}{X_m} U_{s\_\text{Re}} + \frac{\sigma X_r X_s}{X_m} I_{s\_\text{Im}} \right) - j \cdot (\text{sign}(s)) \cdot \left(s \frac{\sigma X_r X_s}{X_m} I_{s\_\text{Re}} \right) \quad (3)$$

where X_s, X_m, and X_r denote the stator reactance, the magnetizing reactance, and the rotor reactance, respectively. σ is the leakage coefficient, which is defined as $(X_s X_r - X_m^2)/X_s X_r$. s is the slip value of the induction generator. Moreover, sign function $\text{sign}(s)$ means that if s is positive, its value becomes 1. Alternatively, if s is negative, its value becomes -1.

According to (2) and (3), the phasor diagram of the stator voltage, the stator current, the rotor voltage, and the rotor current is then shown in Fig. 3. In the supersynchronous mode, the rotor voltage is almost in an opposite phase with respect to

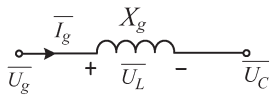

Fig. 4. One-phase L filter of the GSC in the phasor diagram.

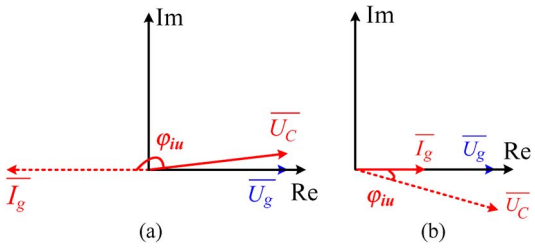

Fig. 5. Phasor diagram of the GSC output voltage and current. (a) Supersynchronous mode. (b) Subsynchronous mode.

the stator voltage, as the slip value is negative. Moreover, the rotor current is almost lagging the rotor voltage 180°, which indicates that the DFIG provides the active power through the rotor side, and the RSC also supplies the excitation energy for the induction generator. In the subsynchronous mode, the rotor current is lagging the rotor voltage less than 90°, implying that the RSC provides both the active power and the reactive power to the induction generator.

For the GSC, if a single inductance is used as a filter, as shown in Fig. 4, by definition of the grid voltage as the reference, the voltage and current relationships between the grid and the converter output are

$$\overline{I_g} = I_{g\_\mathrm{Re}} + jI_{g\_\mathrm{Im}} \tag{4}$$

$$\overline{U_C} = U_{g\_\mathrm{Re}} - X_g \cdot I_{g\_\mathrm{Im}} + j(-X_g \cdot I_{g\_\mathrm{Re}}) \tag{5}$$

where X_g denotes the filter reactance. The phasor diagram of the GSC voltage and current is shown in Fig. 5.

The switching loss in each power device P_{sw} can be calculated as

$$P_{\mathrm{sw}} = \frac{U_{\mathrm{dc}}}{U^*_{\mathrm{dc}}} \cdot f \cdot \left(\sum_{n=1}^{N} \left(E_{\mathrm{on}}\left(|i_a(n)|\right) + E_{\mathrm{off}}\left(|i_a(n)|\right) \right) + \sum_{n=1}^{N} E_{\mathrm{rr}}\left(|i_a(n)|\right) \right). \tag{6}$$

Similarly, as in (1), the first term is the switching loss for the IGBT T_{sw}, and the second term is the switching loss for the freewheeling diode D_{sw}. E_{on} and E_{off} are the turn-on energy and the turn-off energy dissipated by the IGBT, and E_{rr} is the reverse recovery energy dissipated by the diode, which is normally tested by the manufacturer at a certain dc-link voltage U^*_{dc}. It is assumed that the switching energy is proportional to the actual dc-link voltage U_{dc}.

A 2-MW wind turbine system is used as a case study, and its parameters are listed in the Appendix. With the aid of the conventional vector control, the maximum power point tracking is used for the active power reference. If no reactive power compensation is taken into account, the loss breakdown of each power device can be analytically evaluated in terms of the RSC and the GSC, as shown in Fig. 6.

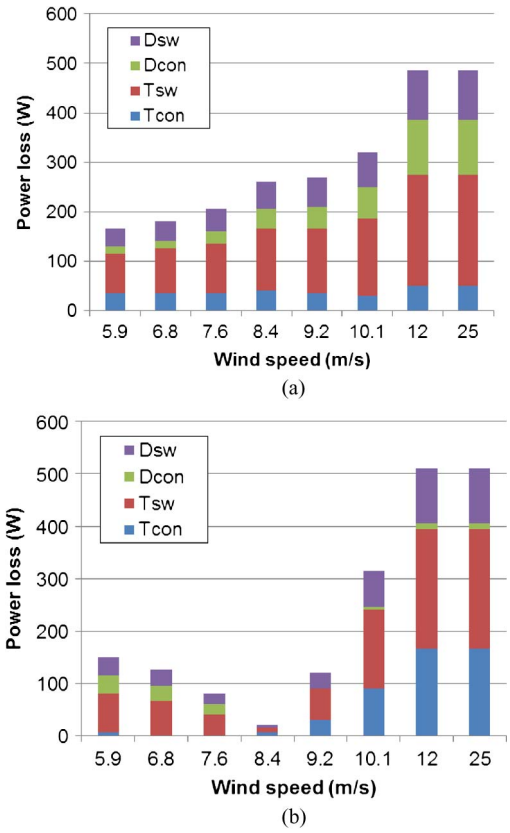

Fig. 6. Loss breakdown of each power device. (a) RSC. (b) GSC.

B. Thermal Cycling of Power Device

The thermal impedance that decides the junction temperature of the power device usually consists of the thermal parameters of the power module itself (from the junction to the baseplate or the case) and the thermal integrate material, as well as the cooling method, as shown in Fig. 7.

Generally, the thermal time constant of a typical air cooling system is from dozens of seconds to hundreds of seconds for a megawatt-level power converter, whereas the maximum thermal time constant of the power device is hundreds of milliseconds. On the other hand, the maximum fundamental period of the power converters' output current is only 1 s, which implies that the thermal cycling caused by the air cooling can be almost neglected [26], [27]. As a result, for the steady-state power cycle analysis, the thermal model of the cooling method will only affect the mean junction temperature but not disturb the junction temperature fluctuation.

As mean junction temperature T_{jm} and junction temperature fluctuation dT_j are commonly regarded as the two most important reliability assessment indicators, their formulas are [28]

$$T_{jm\_T/D} = P \cdot \sum_{i=1}^{4} R_{\mathrm{thjc}\_T/D(i)} + P \cdot \sum_{j=1}^{3} R_{\mathrm{thca}\_(j)} + T_a \tag{7}$$

$$dT_{j\_T/D} = 2P \cdot \sum_{i=1}^{4} R_{\mathrm{thjc}\_T/D(i)} \cdot \frac{\left(1 - e^{-\frac{t_{\mathrm{on}}}{\tau_{\mathrm{thjc}\_T/D(i)}}}\right)^2}{1 - e^{-\frac{t_p}{\tau_{\mathrm{thjc}\_T/D(i)}}}}. \tag{8}$$

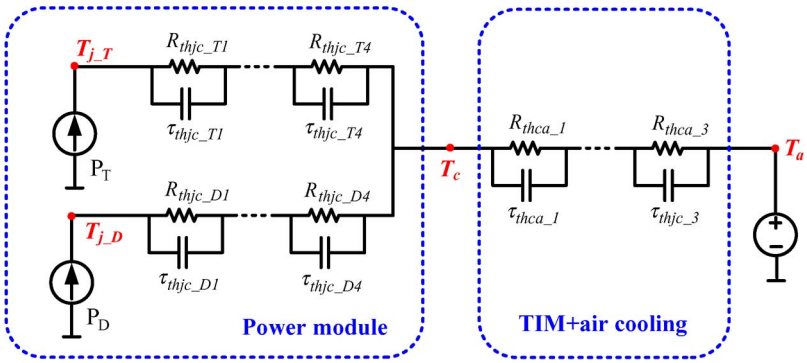

Fig. 7. Thermal model of the power semiconductor for power cycles induced by the fundamental frequency.

In (7), R_{thjc} is the thermal resistance from the junction to the case of the power module, and R_{thca} is the thermal resistance of the air cooling, in which subscripts T and D denote the IGBT and the freewheeling diode, respectively, whereas subscripts i and j denote the four-layer and three-layer Foster structure for the power module and the air cooling, respectively. P is the power loss of each power semiconductor, and T_a is the ambient temperature. In (8), t_{on} denotes the ON-state time within each fundamental period of the current at the steady-state operation, t_p denotes the fundamental period of the current, and τ denotes each Foster layer's thermal time constant.

C. Estimated Lifetime Based on Annual Wind Profile

A power cycling test is defined as follows: The power components are actively heated up by the losses in the semiconductor and cooled down again with the aid of the cooling system. This test can detect the thermomechanical stress between the layers with different thermal expansion coefficients, in which the connection between the chip and the direct bonded copper and the bond wire connection seem to be the most frequent failure mechanisms [14], [15], [26].

In order to accelerate the testing, the introduced current almost equals the rated current of the power semiconductor, and the time cycling is normally between some seconds to dozens of seconds. The values of the power cycles can be obtained at higher junction temperature fluctuations, and then, the values at a lower temperature variation can be extrapolated by the Coffin–Manson equation [16]. Based on the simplified assumption of the uniform failure mechanism over the entire temperature range, the B10 lifetime (10% of the sample components fail if power cycles reach the B10 value) is shown in Fig. 8 with various mean junction temperatures and various junction temperature fluctuations.

Based on (7) and (8), as well as Fig. 6, the steady-state mean junction temperature and junction temperature fluctuation can be calculated at each individual wind speed. Together with the Class-I annual wind speed distribution shown in Fig. 9, in which the velocity increment is 1 m/s, the individual B10 power cycles can be obtained from the cut-in wind speed of 4 m/s to the cutoff wind speed of 25 m/s. In addition, it is worth mentioning the rated wind speed of 11 m/s.

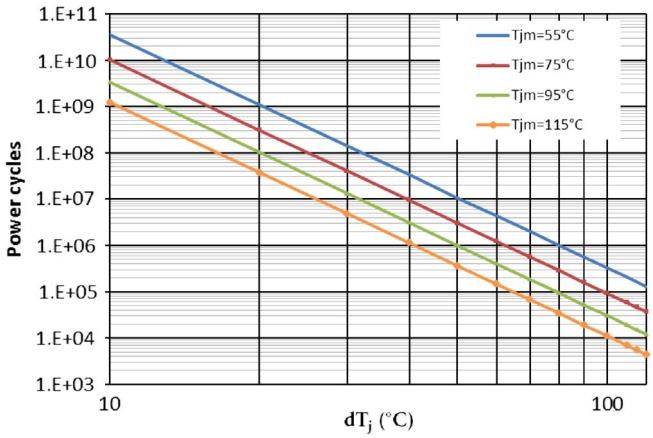

Fig. 8. Example of the fitting power cycle curve versus the mean junction temperature and the junction temperature fluctuation according to the Coffin–Manson model [16].

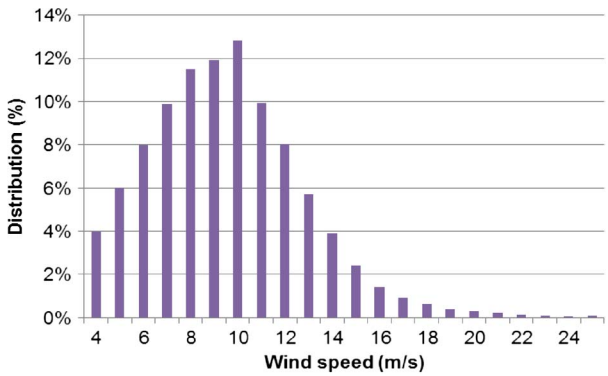

Fig. 9. Class-I annual wind profile according to the IEC standard [33], [34].

The lifetime consumed per year of the IGBT and the freewheeling diode inside the BTB power converters at each wind speed can be calculated as

$$CL_m = D_m \cdot \frac{365 \cdot 24 \cdot 3600 \cdot f_m}{N_m} \tag{9}$$

where D is the annual percentage of every wind speed, f is the fundamental frequency of the output current, and N is the power cycles consistent with Fig. 8. Subscript m denotes the various wind speeds from the cut-in wind speed to the cutoff wind speed.

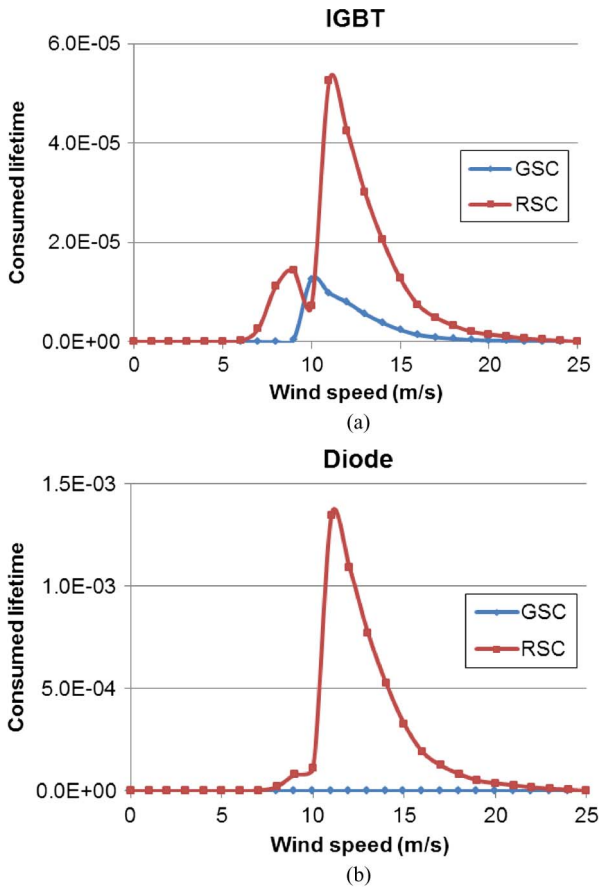

Fig. 10. Consumed lifetime of the switching semiconductors in the BTB power converters at each wind speed if the reactive power is zero. (a) IGBT. (b) Diode. Note: GSC denotes the GSC, and RSC denotes the RSC.

The lifetime consumed per year of the IGBT and the free-wheeling diode are thus shown in Fig. 10(a) and (b), respectively. For the RSC, it can be seen that the diode dominates the lifetime compared with the IGBT, whereas for the GSC, it is the IGBT that has much less lifetime expectancy. Moreover, the lifespan of the RSC is much shorter than that of the GSC.

According to Miner's rule [17], [19], [29], the total consumed lifetime per year can be then estimated by

$$CL = \sum_{m=4}^{25} CL_m. \tag{10}$$

A comparison of the total consumed lifetime between the RSC and the GSC is shown in Fig. 11. It is noted that the lifetime of the BTB power converters becomes very unbalanced, in which the lifetime of the GSC only consumes 1/100 of the RSC. Moreover, due to the orders of magnitude difference between the IGBT and the diode with respect to the total consumed lifetime, for simplicity, the thermal performance of the diode is only focused to estimate the RSC lifetime, whereas the IGBT is only focused to analyze the lifespan of the GSC.

III. Lifetime Reduction to Support Modern Grid Codes

As wind farms are normally located at remote areas, stricter grid codes are issued in order to guarantee a stable grid voltage.

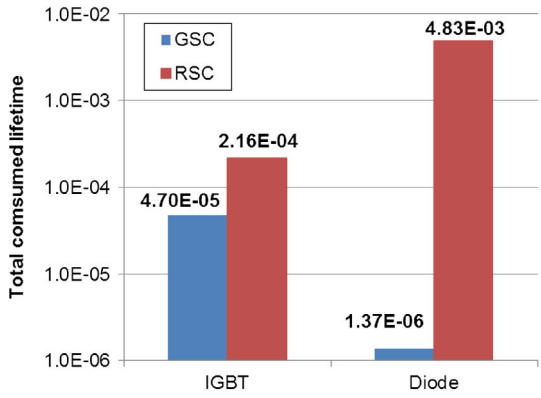

Fig. 11. Total consumed lifetime between the RSC and the GSC.

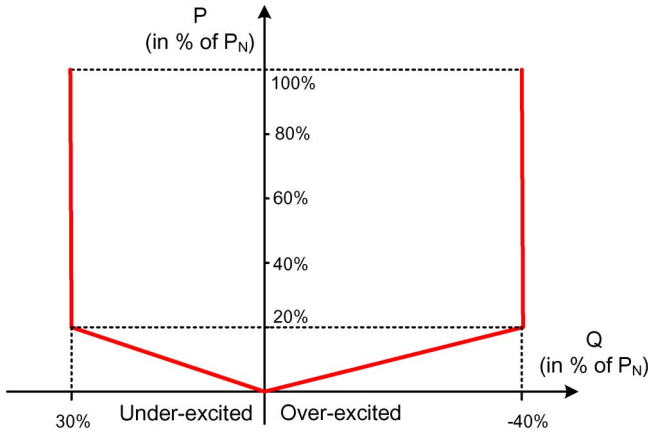

Fig. 12. Reactive power support stated in the German grid code [30].

This section will first describe a modern grid code and then address the additional stress of the power device with respect to the reactive power injection.

A. Modern Grid Codes

As shown in Fig. 12, the most representative grid code with respect to the reactive power regulation is the E.ON requirement for grid connections [30]. If the active power is above 20%, up to 30% of the under-excited reactive power and 40% of the over-excited reactive power are expected to be supported. For the DFIG configuration, it is worth to note that the under-excited reactive power denotes the reactive power absorbed from the grid by the DFIG. Alternatively, the over-excited reactive power denotes the reactive power injected to the grid by the DFIG.

B. Reactive Power Stress on BTB Power Converters

For the RSC, as illustrated in (2) and (3), the rotor current and the rotor voltage of the DFIG are closely related to the generated active power by the wind energy, as well as the reactive power exchange between the DFIG and the grid required by the transmission system operator. Similarly, for the GSC, it is shown in (4) and (5) that the converter current and its interfacing voltage also depend on the active power and the reactive power. As a result, the supportive reactive current introduces additional current stress to the power device and

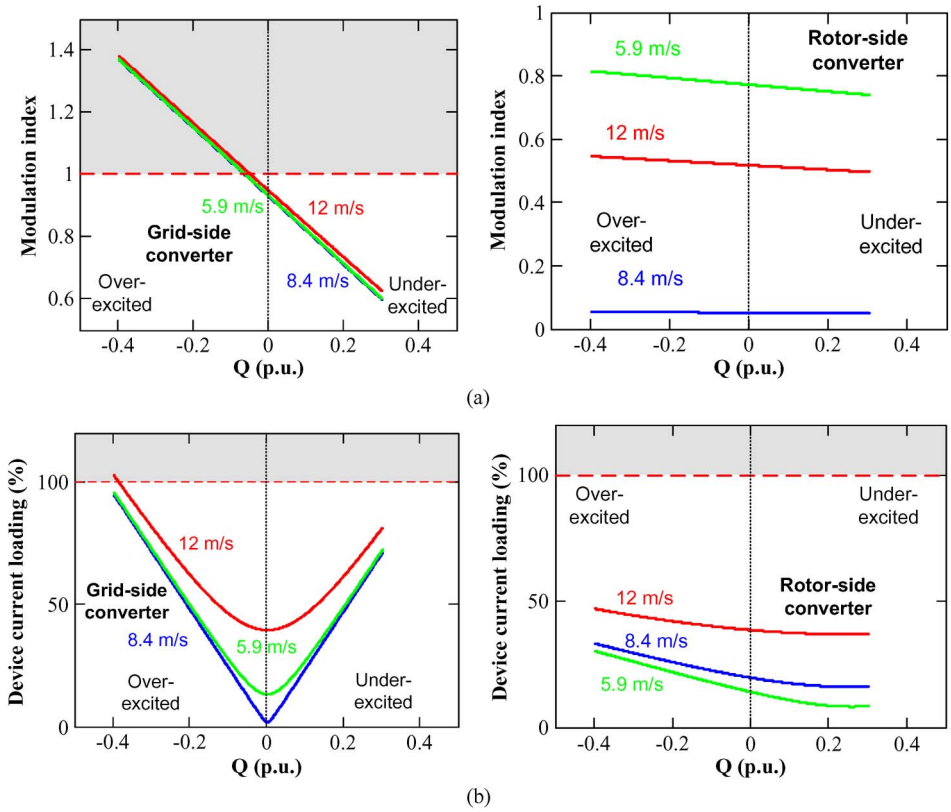

Fig. 13. Effects of the reactive power injection on the current stress and the voltage stress of the power device. (a) Modulation index. (b) Device current loading.

voltage stress in the dc-link voltage for both the RSC and the GSC [27]. As these two factors are tightly linked to the loss dissipation of the power semiconductor, the effects of the reactive power injection on the current stress and the voltage stress of the power device are shown in Fig. 13(a) and (b), respectively, where wind speeds of 12, 8.4, and 5.9 m/s indicate the supersynchronous mode, the synchronous mode, and the subsynchronous mode of the DFIG operation.

For the GSC, the modulation index almost reaches 1.0 at three typical wind speeds when there is no reactive power exchange between the DFIG and the grid. The synchronous mode has the relatively minimum value due to the very small slip power through the power converter. Moreover, the over-excited reactive power stresses the dc-link voltage significantly, whereas the under-excited reactive power relieves because the over-excited reactive power or the under-excited reactive power introduces the same or opposite direction of voltage drop through the filter inductance with respect to the grid voltage, as shown in Fig. 5. Furthermore, either the over-excited reactive power or the under-excited reactive power considerably increases the current loading of the device.

For the RSC, as illustrated in (2) and (3), the rotor voltage is jointly decided by the stator and rotor winding ratio and the slip value of the generator. As a result, the modulation index at different wind speeds is found in Fig. 13(a), in which the highest slip value causes the highest modulation index. With respect to the device loading of the RSC, the situation is also better than the GSC in the case of the reactive power injection. It is interesting to note that the under-excited reactive power injection reduces the current stress of the power device, as under this circumstance, the excitation energy actually is supported by the grid. Because of the ratio between the stator winding and the rotor winding of the induction generator, the variation of the current in each power device is also smaller than in the GSC. Above all, it is more effective to support the reactive power from the RSC compared with the GSC.

TABLE I
DIFFERENT STRATEGIES FOR JOINT REACTIVE POWER COMPENSATION

	RSC (pu)	GSC (pu)	U_{dc}(V)
Case I	0	-0.4	1500
Case II	-0.1	-0.3	1350
Case III	-0.2	-0.2	1200
Case IV	-0.3	-0.1	1100
Case V	-0.4	0	1050

Note: It is assumed that 0.4 pu over-excited reactive power is needed according to the grid codes [30].

IV. JOINT REACTIVE POWER COMPENSATION FROM BTB POWER CONVERTER

As aforementioned, the RSC and the GSC both have the abilities to support the reactive power injection. This section will evaluate the effects of the reactive power flow between the GSC and the RSC seen from the lifetime and the reliable operation points of view.

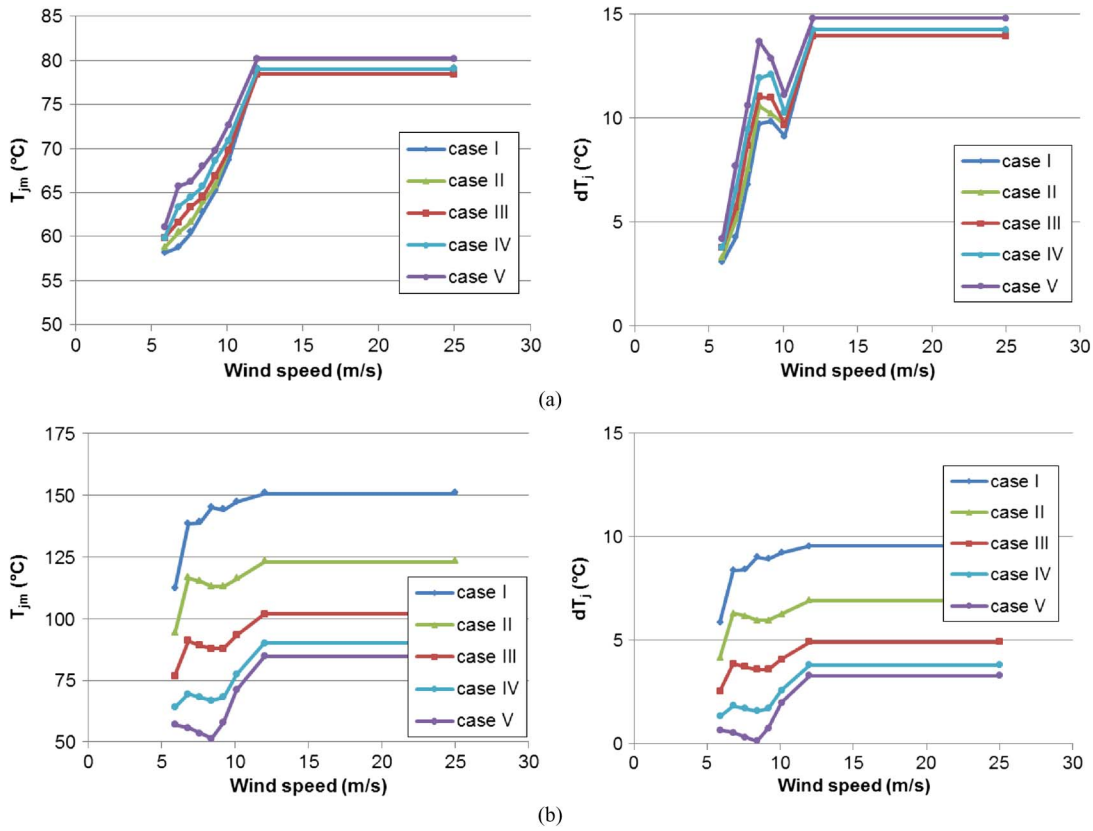

Fig. 14. Thermal profile of the most stressed power semiconductor in terms of the mean junction temperature and the junction temperature fluctuation, where the reactive power is provided with various compensation strategies. (a) Diode in the RSC. (b) IGBT in the GSC.

A. Different Strategies for Joint Reactive Power Compensation

As the overmodulation affects the dynamic performance in the power electronics converter [31], [32], the different control strategies are all realized within the linear modulation range. As shown in Fig. 13, only the over-excited reactive power increases the current stress of the power device in the RSC; thus, it will reduce the lifetime of the RSC. Different load sharing strategies for the over-excited reactive power between the RSC and the GSC can be achieved in Table I, where the dc voltage varies according to the linear modulation range of the GSC.

B. Thermal Behavior of Power Semiconductor

According to (2) and (4), the different amounts of the over-excited reactive power between the RSC and the GSC can be independently expressed by the imaginary part of the stator current and the GSC output current. As a result, the conduction loss and the switching loss of the IGBT and the diode can be calculated. Moreover, substituting the loss information into (7) and (8), the most stressed power semiconductors for the BTB power converters (i.e., the freewheeling diode of the RSC and the IGBT of the GSC) are shown in Fig. 14(a) and (b).

In Fig. 14(a), it is shown that the mean junction temperature and the junction temperature fluctuation insignificantly change among all the compensation strategies. Meanwhile, the diode has the worst thermal behavior in Case V (the reactive power is fully compensated from the RSC), but it has the best thermal performance in Case I (the reactive power is fully compensated from the GSC). In Fig. 14(b), the thermal performance of the IGBT in the GSC at different compensation strategies varies a lot. The worst situation is Case I (the reactive power is fully supported by the GSC), in which the mean junction temperature almost reaches 150 °C.

C. Lifetime Tradeoff Between GSC and RSC

With the thermal profile of the most stressed power semiconductor shown in Fig. 14, as well as the fundamental frequency of the power converter output current and the annual wind speed distribution, the lifetime consumed per year of the individual wind speed is shown in Fig. 15. If the wind speed is above the rated value, it is obvious that the wind speed at 11 m/s has the highest consumed lifetime of the RSC. One of the reasons is that, as the rated wind speed is 11 m/s, the wind speed at 11 m/s has the highest percentage above the rated wind speed, as shown in Fig. 9. The other factor is the same thermal performance above the rated wind speed, as shown in Fig. 14(a). However, if the wind speed is below the rated value, although the 8-m/s wind speed (the synchronous operation of the DFIG) hardly contains the highest percentage, as shown in Fig. 9, it actually consumes the majority lifetime among the wind speeds below the rated value, owing to the fact that the synchronous operation has the largest junction temperature fluctuation below the rated wind speed, as shown in Fig. 14(a). Moreover, the smaller the amount of reactive power it injects from the RSC, the smaller consumed lifetime it can obtain.

For the GSC, the lifetime consumed per year of the individual wind speed significantly changes with different compensation

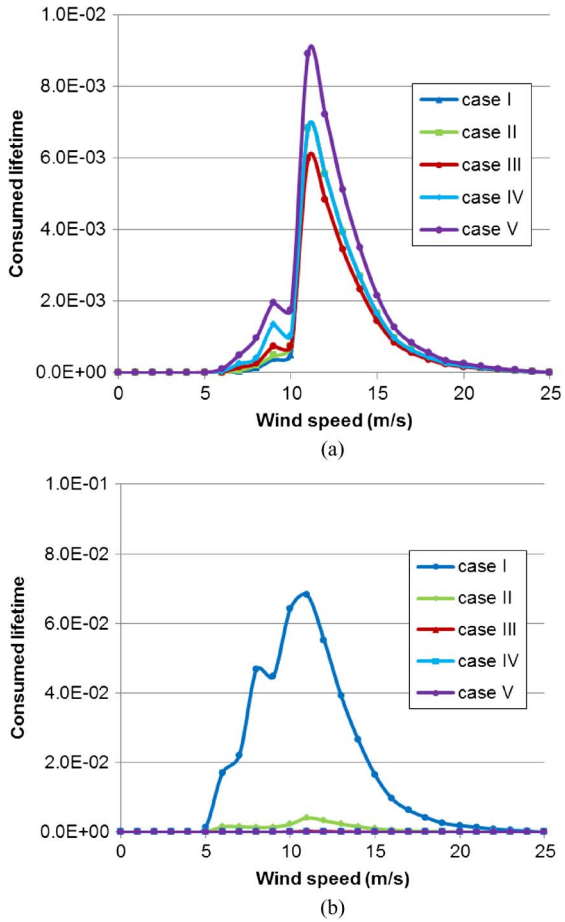

Fig. 15. Consumed lifetime of the most stressed power semiconductor at each wind speed. (a) RSC. (b) GSC.

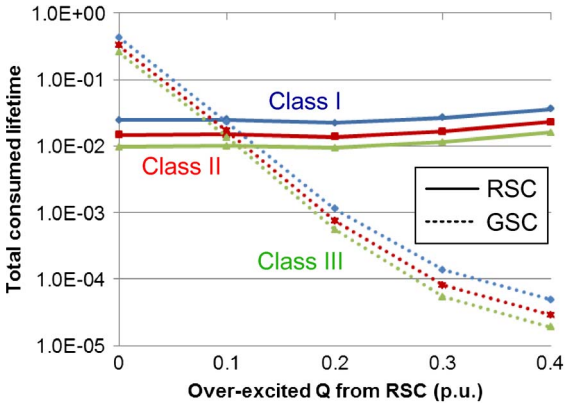

Fig. 16. Total consumed lifetime among the different compensation strategies, in which the various wind classes are also taken into account. Note: The solid line indicates the diode of the RSC, and the dotted line indicates the IGBT of the GSC. Colors blue, red, and green indicate the wind classes Class I, Class II, and Class III, respectively.

strategies. For instance, the highest consumed lifetime at 11 m/s moves from the worst 6.82E-2 in Case I to the best 1.42E-05 in Case V, which implies that the nearly 5000-times difference between them can easily induce the significant variation of the GSC lifetime.

The total consumed lifetime for the five combined reactive power strategies from the GSC and the RSC are shown in Fig. 16 using the log scale, in which three wind classes are

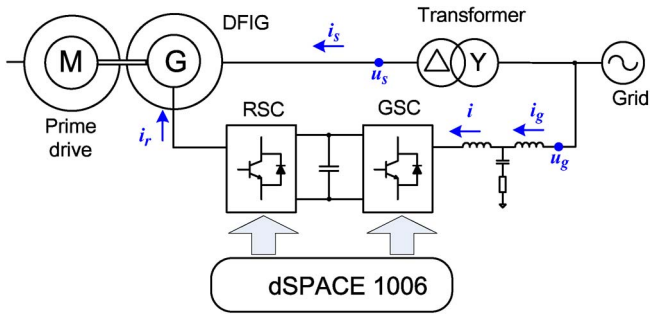

Fig. 17. Setup of the 7.5-kW DFIG system test rig.

also considered. According to the International Electrotechnical Commission (IEC) standard [33], [34], the mean wind speed of Class I, Class II, and Class III is 10, 8.5, and 7.5 m/s, respectively. In the case of the wind Class I, the total consumed lifetime almost stays constant in a log scale at different compensation schemes from the RSC point of view, whereas for the GSC, the total consumed lifetime varies significantly. Moreover, it can be seen that the most balanced lifetime between the RSC and the GSC appears in Case II, in which a 0.1-per unit (p.u.) over-excited reactive power is supported by the RSC, and 0.3 p.u. is provided by the GSC. It is evident that the total consumed lifetime of the RSC can be optimized from 3.59E-2 (Case V) to 2.50E-2 (Case II), which implies a 1.5-times enhanced lifespan. For different wind classes, the tendencies are almost consistent with the Class-I wind.

V. Experimental Results

In order to validate the equations and control strategies, a downscale 7.5-kW test system has been built and is shown in Fig. 17. The DFIG is externally driven by a 0prime motor, and the power electronic converters are linked to the grid through an LCL filter. Two 5.5-kW Danfoss motor drives are used for the GSC and the RSC, both of which are controlled by the implementation of dSPACE 1006. Due to the fact that the junction temperature of the power semiconductor is not easy to be measured, the experimental results are conducted through the electrical characteristics of the DFIG system.

With the parameters of the test system summarized in the Appendix, the reactive power influence on the current stress and the voltage stress of the BTB power converters is analytically calculated, as shown in Fig. 18. It is noted that the tendency of the 7.5-kW DFIG system is similar to the 2-MW system, as shown in Fig. 13, in terms of the modulation index and the current amplitude. Moreover, as the LCL filter significantly reduces the total inductance of the grid filter compared with the pure L-structure filter, the dc link of the test rig is set at 650 V, and this value is high enough to supply a 0.4-p.u. over-excited reactive power even from the GSC, as shown in Fig. 18(a). Rotor speeds at 1050, 1470, and 1800 r/min are selected for the subsynchronous, synchronous, and supersynchronous operations, whose produced active power values are 1, 3, and 5 kW, respectively. Then, the modulation index and the current amplitude can be tested at various amounts of the reactive power requirement.

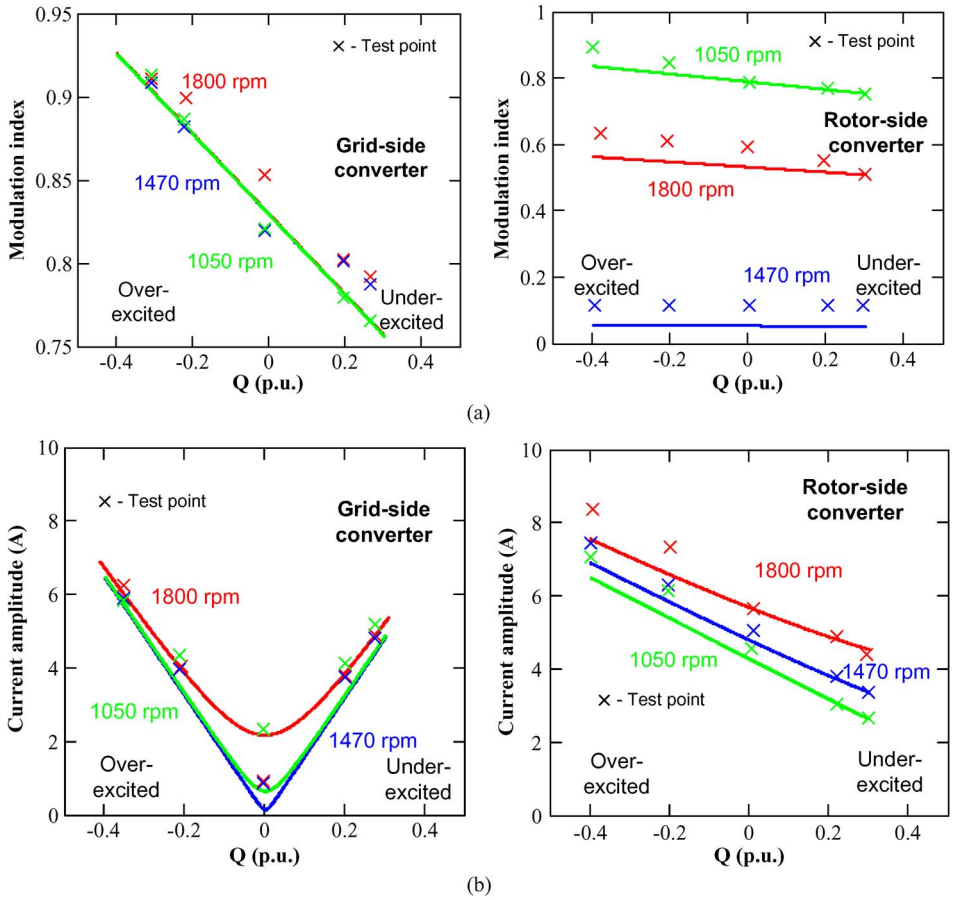

Fig. 18. Experimental validation of the reactive power influence on the current stress and the voltage stress of the BTB power converters. (a) Modulation index. (b) Device current loading. Note: The active power references are 5, 3, and 1 kW in the cases of rotor speeds at 1800, 1470, and 1050 r/min, respectively.

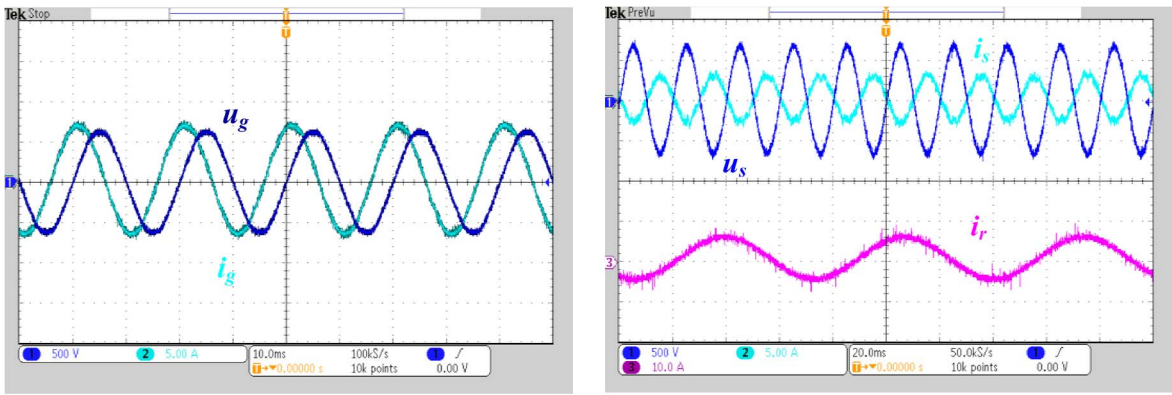

Fig. 19. Experimental result of the DFIG test rig at the subsynchronous speed of 1050 r/min if the 0.4-p.u. over-excited reactive power is fully injected by the GSC. (a) Grid current with respect to the grid voltage. (b) Stator current and the rotor current with respect to the stator voltage.

As the loss of the induction generator can be hardly neglected in the 7.5-kW DFIG, additional current is introduced in the BTB power converters to compensate for the generator loss. As shown in Fig. 18(b), if no reactive power is taken into account, the test result of the GSC is higher than the theoretical value at the subsynchronous mode, whereas the current amplitude is a little lower than the theoretical value at the supersynchronous mode. However, for the RSC, if no reactive power injection is considered, the tested rotor current amplitude is similar to the theoretical value because the active current component is rather small compared with the excitation current. Moreover, the tendencies of the modulation index and the current amplitude of the BTB power converters are consistent with the analytical values. Above all, it is concluded that there is a good correlation between the theory and the experiment if the various amounts of the reactive power are taken into account.

Assuming that the DFIG operates in the subsynchronous mode at 1050 r/min with a 1-kW active power, the full amount of the over-excited reactive power 3 kVar can be provided by either the GSC or the RSC. As shown in Fig. 19, if the

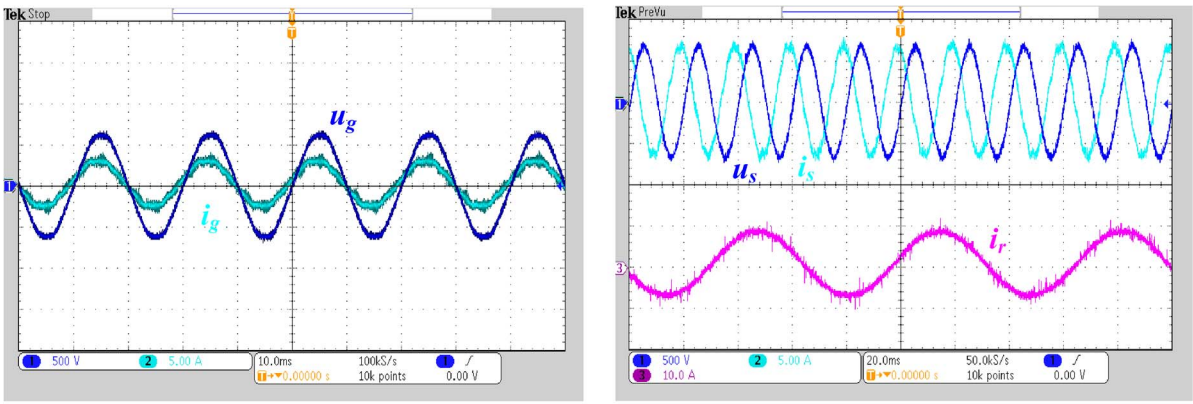

(a) (b)

Fig. 20. Experimental result of the DFIG test rig at the subsynchronous speed of 1050 r/min if the 0.4-p.u. over-excited reactive power is fully injected by the RSC. (a) Grid current with respect to the grid voltage. (b) Stator current and the rotor current with respect to the stator voltage.

reactive power compensation is fully provided by the GSC, the active current component could be rather small compared with the reactive current component due to the slip power flowing through. As a result, the GSC current is almost leading the grid voltage 90°. For the RSC, as the DFIG injects the power to the grid, the stator current and the stator voltage are almost reverse, as expected.

Fig. 20 shows the case when the 0.4-p.u. over-excited reactive power is completely supported by the RSC. The GSC current is exactly in phase with the grid voltage, whereas the stator current is leading the stator voltage 90° due to the dominating reactive current component.

VI. Conclusion

In this paper, the consumed lifetime of the GSC and the RSC in a DFIG system has been first compared based on a typical annual wind profile. If there is no reactive power exchange between the DFIG and the grid, the GSC has more than 100-times lifetime compared with the RSC due to their various control objectives and the various fundamental frequencies of the output current.

The influence of the reactive power support required in modern grid codes is also evaluated for the BTB power converters in terms of the modulation index and the current loading of each device. It is found that the reactive power compensation from the RSC is more effective than the support from the GSC. Moreover, it can be also seen that the over-excited reactive power significantly reduces the lifetime of the RSC.

By introducing an optimized reactive power flow between the GSC and the RSC, the lifetime tradeoff can be achieved; thus, they have a more balanced lifetime. It is concluded that, depending on the specific power converter design, the most appropriate reactive power division between the GSC and the RSC can enhance the lifetime 1.5 times compared with the case where the reactive power is fully provided through the RSC. Furthermore, in order to enhance the reliability, a proper asymmetrical design of the BTB power converters and the chip redesign of the power device could also have a promising potential in the design of the wind power converter.

Appendix
Parameters for the 2-mW and 7.5-kW DFIGs

DFIGs		
Rated power P_n [kW]	2000	7.5
Phase peak voltage U_{sn} [V]	563	311
Stator resistance R_s [mΩ/pu]	1.69/0.007	440/0.023
Stator leakage inductance L_{ls} [mH/pu]	0.04/0.050	3.44/0.056
Rotor resistance R_r [mΩ/pu]	1.52/0.006	640/0.033
Rotor leakage inductance L_{lr} [mH/pu]	0.06/0.085	5.16/0.085
Magnetizing inductance L_m [mH/pu]	2.91/3.840	79.30/1.294
Turns ratio N_s/N_r	0.369	0.336
Power converters		
Rated power [kW]	400	5
DC-link voltage U_{dc} [V/pu]	1050/1.522	650/1.711
Switching frequency f_s [kHz]	2	5
Grid filters		
Boost inductance [mH/pu]	0.5/0.132	18/0.039*

"*" indicates the total inductance of the LCL filter, including both the grid-side inductor and the converter-side inductor.

References

[1] World Wind Energy Association—2013 Half-Year Report. [Online]. Available: http://www.wwindea.org/home/index.php

[2] Y. Li, L. Luo, C. Rehtanz, C. Wang, and S. Ruberg, "Simulation of the electromagnetic response characteristic of an inductively filtered HVDC converter transformer using field-circuit coupling," *IEEE Trans. Ind. Electron.*, vol. 59, no. 11, pp. 4020–4031, Nov. 2012.

[3] F. Blaabjerg, Z. Chen, and S. B. Kjaer, "Power electronics as efficient interface in dispersed power generation systems," *IEEE Trans. Power Electron.*, vol. 19, no. 5, pp. 1184–1194, Sep. 2004.

[4] J. M. Carrasco *et al.*, "Power-electronic systems for the grid integration of renewable energy sources: A survey," *IEEE Trans. Ind. Electron.*, vol. 53, no. 4, pp. 1002–1016, Jun. 2006.

[5] J. M. Guerrero *et al.*, "Distributed generation: Toward a new energy paradigm," *IEEE Ind. Electron. Mag.*, vol. 4, no. 1, pp. 52–64, Mar. 2010.

[6] M. Liserre, R. Cardenas, M. Molinas, and J. Rodriguez, "Overview of multi-MW wind turbines and wind parks," *IEEE Trans. Ind. Electron.*, vol. 58, no. 4, pp. 1081–1095, Apr. 2011.
[7] B. Hahn, M. Durstewitz, and K. Rohrig, "Reliability of wind turbines—Experience of 15 years with 1500 WTs," in *Wind Energy: Proceedings of the Euromech Colloquium*. Berlin, Germany: Springer-Verlag, pp. 329–332.
[8] *Handbook for Robustness Validation of Automotive Electrical/Electronic Modules*, ZVEL, Jun. 2008.
[9] D. Hirschmann, D. Tissen, S. Schroder, and R.W. De Doncker, "Inverter design for hybrid electrical vehicles considering mission profiles," in *Proc. IEEE Conf. Veh. Power Propulsion*, 2005, pp. 1–6.
[10] C. Busca *et al.*, "An overview of the reliability prediction related aspects of high power IGBTs in wind power applications," *Microelectron. Rel.*, vol. 51, no. 9–11, pp. 1903–1907, Sep.–Nov. 2011.
[11] S. Yang *et al.*, "An industry-based survey of reliability in power electronic converters," *IEEE Trans. Ind. Appl.*, vol. 47, no. 3, pp. 1441–1451, May/Jun. 2011.
[12] F. Richardeau and T. T. L. Pham, "Reliability calculation of multilevel converters: Theory and applications," *IEEE Trans. Ind. Electron.*, vol. 60, no. 10, pp. 4225–4233, Oct. 2013.
[13] H. Behjati and A. Davoudi, "Reliability analysis framework for structural redundancy in power semiconductors," *IEEE Trans. Ind. Electron.*, vol. 60, no. 10, pp. 4376–4386, Oct. 2013.
[14] "Load-cycling capability of HiPaks," ABB Application Note. 2004.
[15] A. Wintrich, U. Nicolai, and T. Reimann, Semikron Application Manual, p. 128, 2011.
[16] U. Scheuermann and R. Schmidt, "A new lifetime model for advanced power modules with sintered chips and optimized Al wire bonds," in *Proc. PCIM*, 2013, pp. 810–813.
[17] K. Ma, M. Liserre, F. Blaabjerg, and T. Kerekes, "Thermal loading and lifetime estimation for power device considering mission profiles in wind power converter," *IEEE Trans. Power Electron.*, to be published.
[18] D. Weiss and H. Eckel, "Fundamental frequency and mission profile wearout of IGBT in DFIG converters for windpower," in *Proc. EPE*, 2013, pp. 1–6.
[19] H. Wang, M. Liserre, and F. Blaabjerg, "Toward reliable power electronics: Challenges, design tools, and opportunities," *IEEE Ind. Electron. Mag.*, vol. 7, no. 2, pp. 17–26, Jun. 2013.
[20] H. Wang, D. Zhou, and F. Blaabjerg, "A reliability-oriented design method for power electronic converters," in *Proc. APEC*, 2013, pp. 2921–2928.
[21] B. Cezar Rabelo, W. Hofmann, J. L. da Silva, R. G. de Oliveira, and S. R. Silva, "Reactive power control design in doubly fed induction generators for wind turbines," *IEEE Trans. Ind. Electron.*, vol. 56, no. 10, pp. 4154–4162, Oct. 2009.
[22] D. P. Bagarty and D. Kastha, "Reactive power allocation for loss minimization in a stand-alone variable speed constant frequency double output induction generator," *IET Power Electron.*, vol. 6, no. 5, pp. 851–861, May 2013.
[23] T. B. Soeiro and J. W. Kolar, "Analysis of high-efficiency three-phase two- and three-level unidirectional hybrid rectifiers," *IEEE Trans. Ind. Electron.*, vol. 60, no. 9, pp. 3589–3601, Sep. 2013.
[24] D. Zhou, F. Blaabjerg, M. Lau, and M. Tonnes, "Thermal analysis of multi-MW two-level wind power converter," in *Proc. IEEE IECON*, 2012, pp. 5862–5868.
[25] K. Zhou and D. Wang, "Relationship between space-vector modulation and three-phase carrier-based PWM: A comprehensive analysis," *IEEE Trans. Ind. Electron.*, vol. 49, no. 1, pp. 186–196, Feb. 2002.
[26] D. Zhou, F. Blaabjerg, M. Lau, and M. Tonnes, "Thermal cycling overview of multi-megawatt two-level wind power converter at full grid code operation," *Inst. Elect. Eng. Jpn. Trans. Ind. Appl.*, vol. 2, no. 4, pp. 173–182, Jul. 2013.
[27] M. Marz and P. Nance, Thermal Modeling of Power-Electronic System. [Online]. Available: http://www.infineon.com/
[28] D. Zhou, F. Blaabjerg, M. Lau, and M. Tonnes, "Thermal profile analysis of doubly-fed induction generator based wind power converter with air and liquid cooling methods," in *Proc. EPE*, 2013, pp. 1–10.
[29] M. A. Miner, "Cumulative damage in fatigue," *J. Appl. Mech.*, no. 12, pp. A159–A164, 1945.
[30] E. ON-Netz, Requirements for Offshore Grid Connections, Apr. 2008.
[31] D. Zhou, F. Blaabjerg, M. Lau, and M. Tonnes, "Thermal behavior optimization in multi-MW wind power converter by reactive power circulation," *IEEE Trans. Ind. Appl.*, vol. 50, no. 1, pp. 433–440, Jan./Feb. 2014.
[32] S. Busquets-Monge, R. Maheshwari, and S. Munk-Nielsen, "Overmodulation of n-level three-leg DC-AC diode-clamped converters with comprehensive capacitor voltage balance," *IEEE Trans. Ind. Electron.*, vol. 60, no. 5, pp. 1872–1883, May 2013.
[33] *Wind Turbines—Part I: Design Requirements*, IEC 61400-1, 2005, 3rd edition.
[34] Vestas website. [Online]. Available: http://www.vestas.com/en/wind-power-plants/wind-project-planning/siting/wind-classes.aspx?action=3#/vestas-univers

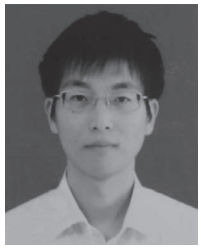

Dao Zhou (S'12) received the B.Sc. degree in electrical engineering from Beijing Jiaotong University, Beijing, China, in 2007 and the M.Sc. degree in power electronics from Zhejiang University, Hangzhou, China, in 2010. He is currently working toward the Ph.D. degree in the Department of Energy Technology, Faculty of Engineering and Science, Aalborg University, Aalborg, Denmark.

His research interests include two-level power electronics converters and their application in wind power generation systems.

Frede Blaabjerg (S'86–M'88–SM'97–F'03) received the Ph.D. degree from Aalborg University, Aalborg, Denmark, in 1992.

From 1987 to 1988, he was with ABB-Scandia, Randers, Denmark. In 1992, he became an Assistant Professor with Aalborg University, where he became an Associate Professor in 1996 and has been a Full Professor of power electronics and drives with the Department of Energy Technology, Faculty of Engineering and Science, since 1998. His current research interests include power electronics and applications in wind turbines, photovoltaic systems, reliability, harmonics, and adjustable-speed drives.

Dr. Blaabjerg was Editor-in-Chief of the IEEE TRANSACTIONS ON POWER ELECTRONICS from 2006 to 2012. He was a Distinguished Lecturer of the IEEE Power Electronics Society from 2005 to 2007 and of the IEEE Industry Applications Society from 2010 to 2011. He was the recipient of 15 IEEE Prize Paper Awards, the IEEE Power Electronics Society (PELS) Distinguished Service Award in 2009, the International Power Electronics and Motion Control Conference (EPE-PEMC) Council Award in 2010, the IEEE William E. Newell Power Electronics Award in 2014, and the Villum Kann Rasmussen Research Award in 2014.

Mogens Lau received the M.Sc. degree in electrical engineering from Aalborg University, Aalborg, Denmark, in 1999.

He worked as a Development Engineer, as a Project Manager, and as a Line Manager for power electronics with leading companies such as Siemens A/S, Danfoss A/S, Grundfoss, and Vestas Wind Systems A/S. He is currently with Siemens Wind Power A/S, Brande, Denmark.

Michael Tønnes received the M.Sc. degree in electrical engineering and the Ph.D. degree from Aalborg University, Aalborg, Denmark, in 1987 and 1990, respectively.

In 1987, he was employed by Danfoss A/S to perform his Ph.D. work on the autotuning and automatic control of nonlinear electrical machines, and he worked within the technology area of motor controls. From 1996 to 1998, he worked in the USA with Danfoss High Power Drives and has over the years had various management positions within electronic businesses. Currently, he is the Senior Director of Research and Development with Danfoss Silicon Power GmbH, Flensburg, Germany. He is the author or coauthor of a number of articles on autotuning, motor controls, and power electronics in general, and he is the holder of several patents within the field of motor controls and power electronics.